Geophys. J. Int. (2001) **145,** 579–592

Scattering behaviour at Merapi volcano (Java) revealed from an active seismic experiment

Ulrich Wegler* and Birger-G. Lühr

GeoForschungsZentrum Potsdam, Telegrafenberg Haus E, 14474 *Potsdam, Germany*

Accepted 2000 November 14. Received 2000 November 7; in original form 2000 April 23

SUMMARY

The seismic structure of the stratovolcano Merapi (Java, Indonesia) was studied using an active seismic experiment. Three 3 km long seismic profiles each consisting of up to 30 three-component seismometers with an interstation distance of 100 m were built up in an altitude range between 1000 and 2000 m above sea level. The detailed study of the seismic properties of the propagation media in active volcanic regions is important to understand the natural seismic signals used for eruption forecasting. The seismic experiment at Merapi therefore concentrates on the heterogeneous structure within a radius of 5 km from the active dome, where the sources of most of the natural volcanic seismic events are located. The cone of Merapi volcano consists of different materials changing on a small scale due to the layering of eruptive material. Additionally, the topography of the erosion valleys leads to an irregular deposition, which cannot be described by a simple 1-D layering. These inhomogeneities have a strong influence on seismic signals. The direct *P* and *S* waves are attenuated quickly and show only small amplitudes on seismograms. The energy lost from the direct waves, however, is not changed into heat but scattered and can be observed as seismic coda following the direct waves. The observed seismograms show a spindle-like amplitude increase after the direct *P* phase. This shape of the envelope can be explained by the diffusion model. According to this model there are so many strong inhomogeneities that the direct wave can be neglected and all energy is concentrated in multiple scattered waves. Besides the envelope, the coherence and polarization properties of the wavefield also indicate strong scattering. Only the first onset shows coherence over a station spacing of 100 m, whereas the late phases carrying the major part of the energy are mainly incoherent. The horizontal components of the seismograms have larger amplitudes than the vertical component, but within the horizontal plane the polarization is almost arbitrary, corresponding to waves arriving from scatterers located arbitrarily in space. As a result of the inversion using the diffusion model we obtain values of the *S*-wave scattering attenuation coefficient, η_s, and the *S*-wave intrinsic absorption coefficient, η_i. In the frequency range of 4–20 Hz used in this study the scattering attenuation is at least one order of magnitude larger than the intrinsic absorption ($\eta_s \gg \eta_i$). The mean free path of *S* waves is as low as 100 m ($\eta_s^{-1} \approx 100$ m). The scattering coefficient is independent of frequency ($\eta_s \sim f^{0.0}$), whereas the coefficient of intrinsic attenuation increases with increasing frequency ($\eta_i \sim f^{1.6}$). The natural seismic signals at Merapi volcano show similar characteristics to the artificial shots. The first onsets have only small amplitudes and the energy maximum arrives delayed compared to the direct waves. Therefore, these signals appear to be strongly affected by multiple scattering also.

Key words: scattering, seismic coda, seismology, volcanic structure.

* Now at: Tohoku University, Department of Geophysics, Graduate School of Science, Aoba-Ku, Sendai-Shi, Miyagi-Ken 980-8578, Japan. E-mail: uli@zisin.geophys.tohoku.ac.jp

1 INTRODUCTION

The volcanism of Java is a typical example of volcanism generated by an active ocean island arc system, where the Indo-Australian Plate is subducted below the Eurasian Plate (Wilson 1989, p. 155). Merapi Volcano is one of the many active volcanoes aligning parallel to the Java trench (Fig. 1) and its volcanic products are mainly basaltic andesites (Purbawinata *et al.* 1996; p. 15; Gertisser & Keller 1998). Due to the dense population near the volcano, a high risk from 'nuée ardente' and possible larger explosive eruptions exists. For this reason, Merapi volcano was selected as one of the decade volcanoes during the International Decade for Natural Disaster Reduction (IDNDR) (Newhall *et al.* 1994).

Monitoring the activity of Merapi is the responsibility of the Volcanological Survey of Indonesia (VSI). One of the most important parameters for estimating the probability of an eruption is the seismicity (Ratdomopurbo 1995, pp. 78–89, 171; Purbawinata *et al.* 1996, pp. 18–21; Zschau *et al.* 1998). Natural seismicity is also used at other volcanoes for eruption forecasting (Mori 1995). Ratdomopurbo (1995, pp. 25–37) classified the seismic signals observed at Merapi volcano as A-type, B-type, multiple phase events, long-period events, tremor and rock fall. The physical mechanisms of the different signals, however, are still under discussion. Therefore, the next step towards enhanced eruption forecasting is the understanding of the physical sources of the observed seismic signals.

Within the Indonesian–German joint project MERAPI dealing with the interdisciplinary exploration of the Merapi volcano (Zschau & Westerhaus 1998) there are two seismic experiments. One consists of an enhanced observation of the natural seismic signals using broad-band seismometers and array techniques. The main goals here are automatic detection and classification (Ohrnberger *et al.* 1999) as well as automatic location of the events (Wassermann *et al.* 1999). Since neither the seismic source of the signals nor the propagation medium are known sufficiently, it is uncertain if the observed complexity of the seismograms is caused by a complex source, a complex propagation medium or the local site response near the receiver. This is a common problem in volcano seismology (e.g. Wegler & Seidl 1997). Therefore, at Mt Merapi a second seismic experiment was carried out using artificial seismic sources.

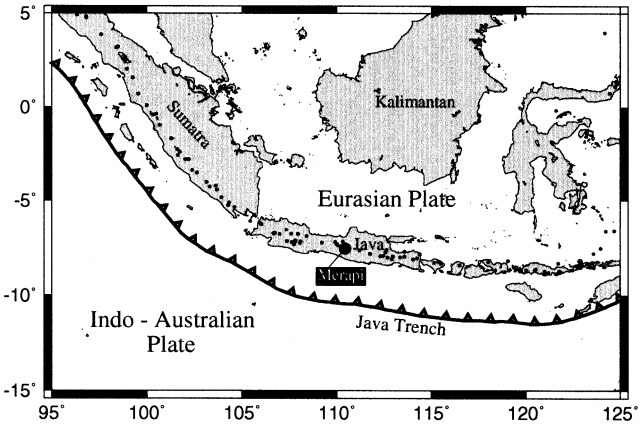

Figure 1. Location of Merapi volcano in southeast Asia. The Java trench marks the boundary of the Indo-Australian and Eurasian plates. Small dots correspond to locations of volcanoes active during the last 10 000 yr (Simkin *et al.* 1981, pp. 50–62). The large dot marks the location of Mt Merapi.

Besides the *P*- and *S*-wave velocity structure, the parameters describing the intrinsic absorption and especially the scattering properties are important seismic quantities of the volcanic edifice. The attenuation can be determined using direct waves or coda waves. The simplest model to describe the coda is the single scattering model (Aki & Chouet 1975; Sato 1977). This model was used to determine the attenuation at Mt St Helens (Fehler *et al.* 1988). Patanè *et al.* (1994) measured the attenuation of the direct wave at Etna volcano. Evans & Zucca (1988) and Yamamoto & Ida (1997) used the direct waves for attenuation tomography at volcanoes. However, it is not possible to separate scattering from intrinsic absorption using direct waves or the single scattering model for coda waves. This separation became possible after the development of suitable multiple scattering models. Mayeda *et al.* (1992) used local earthquakes and the method of 'multiple lapse time window analysis' (Hoshiba 1991; Fehler *et al.* 1992) to separate scattering and intrinsic absorption in Hawaii and Long Valley Caldera (USA). According to this study, for frequencies below 6 Hz intrinsic attenuation dominates, whereas scattering attenuation dominates above 6 Hz. The authors found a mean free path of 20–50 km. Londoño (1996) applied the same method to Nevado del Ruiz volcano (Colombia) and found dominant scattering attenuation above 6 Hz and a mean free path of 10–25 km. Del Pezzo *et al.* (1995, 1996) tried to separate scattering and intrinsic absorption by simultaneous measurements of coda Q and the attenuation of direct waves. Following these authors the volcanic regions of Mt Etna and Campus Flegrei (Italy) show stronger scattering attenuation, whereas in the Granada region (Spain) intrinsic absorption dominates. These authors state a strong influence of the scattering on the observed seismograms. Most researchers use local earthquakes to estimate the attenuation; only a few studies use artificial seismic signals. Nishimura *et al.* (1997) examined the Jemez Volcanic Field (USA) using three explosion sources. Assuming single isotropic scattering, they resolved a strongly scattering region below Valles Caldera.

In this paper we report the results of an experiment using active seismic sources at Mt Merapi Volcano (Java, Indonesia). Since in the case of artificial sources the source signal is well known, we can study in detail the propagation effects of the complex medium, whereas usually the source signal of the volcanic earthquakes as well as the propagation medium are unknown. We find that scattering has an important influence on the observed seismograms. After describing the experimental design we show the most important characteristics of the seismograms. The shape of the envelopes as well as the coherence and polarization properties indicate multiple scattering effects. For that reason in the next Section 4 we apply the diffusion model to the data. We use three different inversion methods to fit the data to the diffusion model. First, we invert the data in the time domain, which yields the most reliable results. Second, we check the results using an independent inversion in the space domain. Third, we use the decay of the energy maximum. In the discussion we comment on the effects of the multiple scattering on the signals of natural seismic events recorded at Merapi volcano.

2 EXPERIMENTAL DESIGN

Fig. 2 shows the locations of the seismic sources and receivers used in the active experiment. The seismic source points at an altitude of 1000 m above sea level form a triangle enclosing

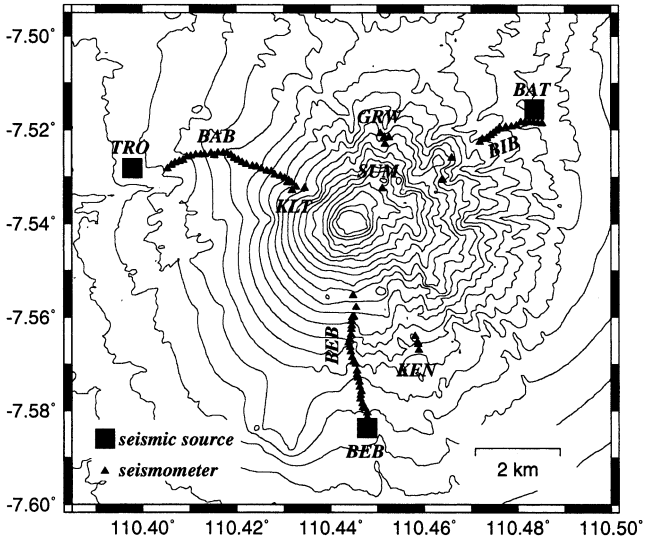

Figure 2. Map of Merapi volcano including the locations of the three seismic sources BEB, TRO and BAT (squares), the three seismic profiles BEB, BAB and BIB, as well as the continuously running seismometer arrays KLT, KEN, GRW and SUM (triangles).

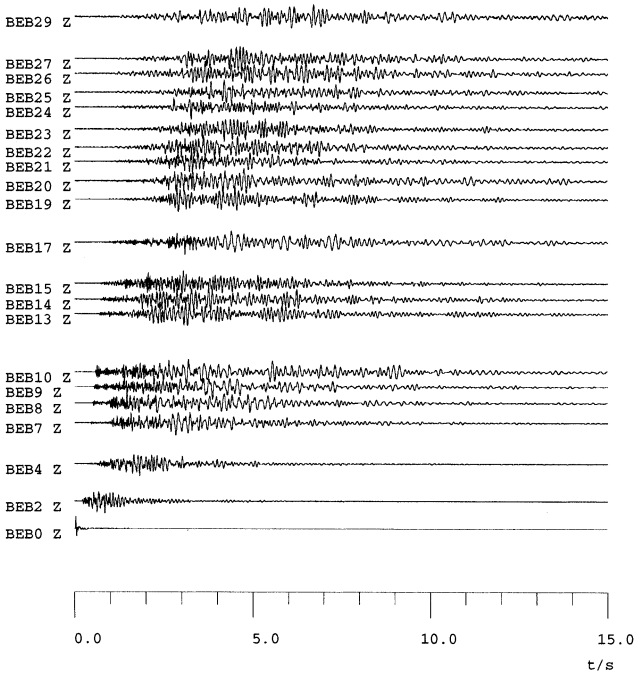

Figure 3. Stacked seismograms (vertical component) of shots from the source BEB recorded at the profile BEB in an offset range between 4 m (BEB0) and 2.957 km (BEB29). The representation is distance-dependent, with each trace normalized to its maximum amplitude.

the volcano. The distance to the active summit region, at an altitude of almost 3000 m above sea level, is approximately 5 km. Each source consists of a rectangular water basin of 2 m × 4 m cross-section and 4.5 m depth equipped with a 2.5 l mudgun. We shot the airguns at pressures around 8 MPa and with shot intervals around 2 min. At each seismometer the repeated shots were recorded between 20 and 120 times. The signals were stacked after deleting traces with severe seismo-volcanic background noise. Wegler *et al.* (1999) and Wegler (1999, pp. 10–18) discussed this special source in more detail. The mudgun signals with a spectral range of between 4 and 25 Hz were recorded on three seismic profiles, each consisting of three-component 1 Hz seismometers with a station spacing of 100 m. The profiles BEB and BAB consisted of 30 seismometers leading to a profile length of 3 km, whereas BIB consisted of 15 seismometers with a length of 1.5 km. Profile BIB was extended by two single stations to a total length of almost 3 km. The profiles cover the altitude range between 1000 and 2000 m above sea level. The locations were measured by a combination of two-phase GPS and a laser tachymeter leading to a spatial accuracy of less than 1 m. In time the wavefield was sampled using a digitization frequency of 250 Hz. Additionally, the shots were recorded at the permanent monitoring arrays GRW, KEN and KLT, but here with a sampling rate of 50 Hz. Each of these arrays consists of one broad-band seismometer and three 1 Hz seismometers with a mean station distance of about 150 m (Wassermann *et al.* 1999).

3 OBSERVATIONS

One of the most impressive characteristics of the seismograms measured at Mt Merapi is their envelopes (Figs 3–5). The strongest amplitudes in the recordings are not caused by the direct *P* and *S* waves, but the main part of the energy is shifted to the late part of the seismograms. Following the first onset, which usually has a very small amplitude, the energy slowly and continuously increases to a maximum value. The direct *S* wave can only be detected up to a maximum offset of 900 m. The late part of the seismogram, following the energy maximum, can be described by an exponential decay. This spindle-like envelope with a delay time of several seconds of the energy

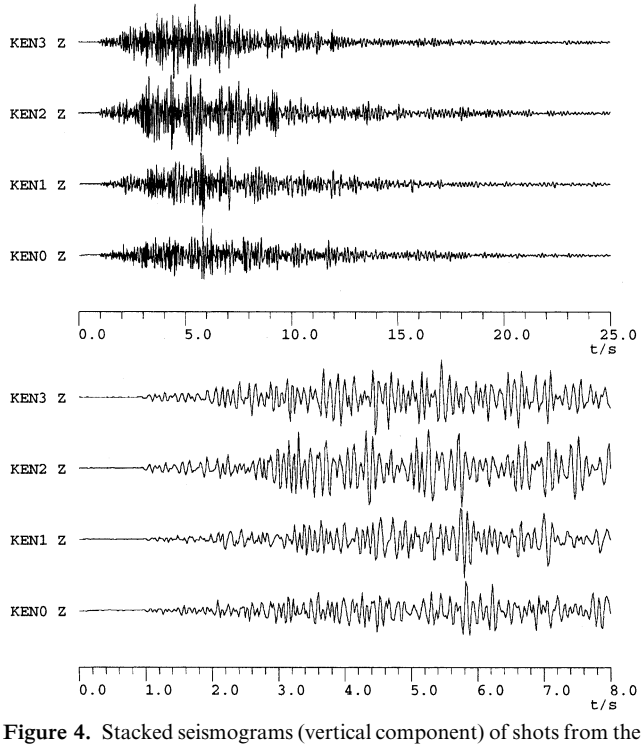

Figure 4. Stacked seismograms (vertical component) of shots from the source BEB recorded at the monitoring array KEN in an offset range between 2.218 km (KEN3) and 2.463 km (KEN1). The mean distance between the stations is about 150 m. Top: 25 s window; bottom: the first 8 s.

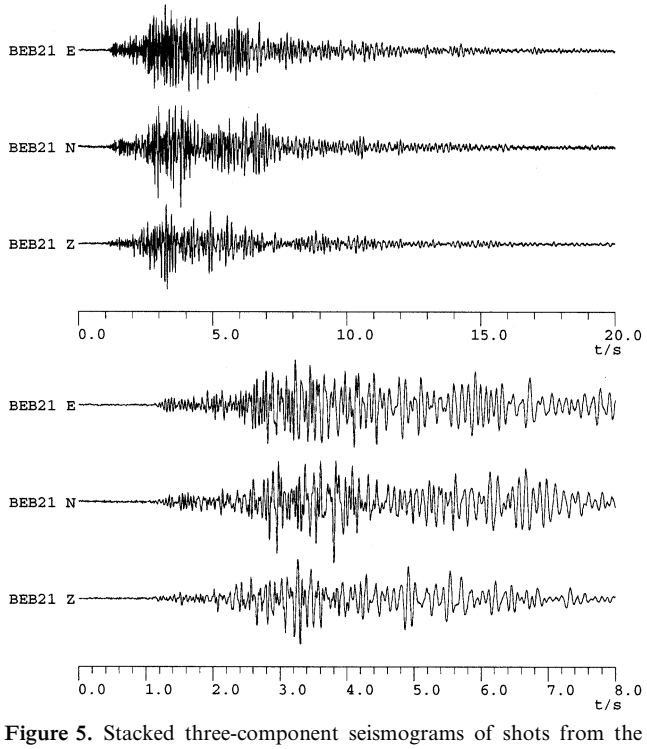

Figure 5. Stacked three-component seismograms of shots from the source BEB recorded at station BEB21 at a distance of 2.104 km. Top: 20 s window; bottom: the first 8 s. Both representations are normalized to true amplitude.

maximum cannot be interpreted by the short radiation of the artificial source, which has a source time as short as 0.25 s (BEB0 in Fig. 3). The group velocity of the energy maximum along one seismic profile is around 300 m s^{-1} depending on frequency and the profile.

The second important characteristics of the wavefield are its coherence and polarization properties. Fig. 4 shows the recorded signals at a monitoring array. Although the inter-station distances are as low as 150 m, the signals vary significantly from one station to another. The late-arriving phases carrying most of the energy are mainly incoherent for the frequencies of 4–20 Hz used in this study, whereas the direct *P* wave is coherent within the array. The polarization properties are also complicated. The different components of one station seem to be almost uncorrelated (Fig. 5). Carrying out a polarization analysis we generally obtain a slight dominance of the horizontal components over the vertical component and almost random values for the polarization within the horizontal plane. The direct *P* wave, in contrast, is mainly vertically polarized.

The unusual envelope shape of the seismogram as well as the coherence and polarization properties can be explained by multiple scattering in the heterogeneous shallow structure of Merapi volcano.

4 DIFFUSION MODEL

The energy density $W(\mathbf{r}, t)$ of a direct body wave expanding from the source can be approximated by the following equation:

$$W(\mathbf{r}, t) = E_0\,\delta(r - vt)\,\frac{1}{4\pi r^2}\exp[-(\eta_s + \eta_i)r]\,, \qquad (1)$$

where η_s and η_i describe the energy loss due to scattering and intrinsic attenuation respectively. In the case of scattering attenuation the energy lost by the direct wave is not converted to other forms of energy but saved as seismic energy. The scattered phases, also referred to as coda, can then be observed in the seismogram following the direct waves. If strong multiple scattering occurs, the amplitude of the coda can even be larger than the amplitude of the direct waves. This effect was intensively studied using seismic records from the moon (Nakamura 1977; Dainty & Toksöz 1981, 1977). The moon seismograms, similar to seismograms recorded at Mt Merapi, show only very small deterministic phases at the beginning of the seismogram. The energy then increases continuously to a maximum and slowly decreases. Additionally, it is a well-known fact that stratovolcanoes are very heterogeneous. Alternating deposits of pyroclastic flows, lahars, ash falls and lava flows form strong impedance contrasts for seismic waves and cause scattering effects. To explain the unusual characteristics of the seismograms observed at Merapi volcano, we therefore suggest a model of strong scattering.

In the case of strong scattering, the scattered wavefield cannot be approximated as a small disturbance of the direct waves as assumed in the Born approximation. As an alternative, the energy transfer theory is used (Wu 1985; Zeng *et al.* 1991; Zeng 1993), where instead of the amplitudes of the waves the transport of energy in the scattering medium is examined, neglecting the phase information. Using such models for multiple scattering it became possible to distinguish between intrinsic and scattering attenuation (Wu 1985). To model the seismograms observed at Mt Merapi the general energy transport theory of Zeng *et al.* (1991) may be used. A second possibility is to use the diffusion model. This model is the asymptotic model of the general theory for very strong scattering, where strong scattering means that the time t is much larger than the mean free time $[t \gg (\eta_s\beta_0)^{-1}]$. Sato (1993) showed analytically that in the 1- and 2-D cases the general theory converges for large times to the diffusion solution. In 3-D space, Gusev & Abubakirov (1987) demonstrated the convergence using the Monte Carlo simulation. Restricting the model to strong scattering makes the equations less complex. First, the variation of energy in time and space using the diffusion model is described by an analytical equation, whereas in the general case two numerical integrations (Zeng *et al.* 1991) or a Monte Carlo simulation (Gusev & Abubakirov 1996, 1987; Hoshiba 1991) are necessary. Additionally, the diffusion solution can be linearized allowing a simple linear inversion. Using this model the following equation describes the density of seismic energy as a function of space and time (Dainty & Toksöz 1981):

$$W(\mathbf{r}, t) = E_0(4\pi dt)^{-p/2}\exp\left[-bt - \frac{r^2}{4dt}\right], \qquad (2)$$

where $W(\mathbf{r}, t)$ is the (theoretical) energy density at location $\mathbf{r}$ and time t, E_0 is the source energy, $p = 3$ for body waves, $p = 2$ for surface waves, d is the diffusivity and b is the (temporal) coefficient for intrinsic attenuation. For reasons discussed later we assume the dominance of *S* waves, i.e. $p = 3$. If we have *a priori* information about the background *S*-wave velocity β_0, we can replace the diffusivity d and the (temporal) coefficient for intrinsic attenuation b by the coefficient for scattering attenuation η_s and the (spatial) coefficient for intrinsic

attenuation η_i,

$$\eta_s = \frac{\beta_0}{p\,d}\,, \qquad (3)$$

$$\eta_i = \frac{b}{\beta_0}\,.$$

Both representations are important. Using d and b does not require knowledge about the background S-wave velocity β_0; however, these two quantities have different dimensions, whereas η_s^{-1} and η_i^{-1} both have the dimension of length so that we can compare the effect of intrinsic attenuation to the effect of scattering attenuation. Moreover, we can compare these values to other length scales such as the source–receiver distance r. The diffusion model assumes strong scattering ($r \gg \eta_s^{-1}$), isotropic scattering, and a space independence of the diffusivity d and the (temporal) coefficient for intrinsic attenuation b (Dainty & Toksöz 1981). In general, the source energy E_0 as well as the diffusivity d and the coefficient for intrinsic attenuation b depend on frequency. Therefore, eq. (2) must hold for each frequency band. This model was first applied to seismic data by Wesley (1965) and later used to explain the seismograms recorded on the moon (Nakamura 1977; Dainty & Toksöz 1981, 1977).

4.1 Temporal variation of energy

By taking the logarithm and multiplying by the geometrical factor $t^{p/2}$, the diffusion model can be linearized. Additionally, we introduce a reference energy density W_1 and a reference time t_1. We choose the reference distance r_1, where $W_1(r_1, t_1) = 1\ \mathrm{J\ m^{-3}}$ for $t_1 = 1$ s (that is, $W_1 = 1\ \mathrm{J\ m^{-3}}$ and $t_1 = 1$ s). Then eq. (2) becomes

$$\ln[H(t)] = a_1 + a_2 t + a_3 \frac{1}{t}\,, \qquad (4)$$

with

$$H(t) = \frac{W(\mathbf{r}, t)}{W_1}\left(\frac{t}{t_1}\right)^{p/2},$$

$$a_1 = \ln\left[\frac{E_0}{W_1}\,(4\pi d t_1)^{-p/2}\right], \qquad (5)$$

$$a_2 = -b\,,$$

$$a_3 = -\frac{r^2}{4d}\,.$$

Now the quantity $\ln[H(t)]$ as a function of time depends only linearly on the three base functions 1, t and $1/t$. Applying the standard method of least squares (Press *et al.* 1988, pp. 534–538) we can compute the three unknown parameters a_1, a_2 and a_3. After the inversion we compute the physically interesting parameters using the following equations:

$$b = -a_2\,,$$

$$d = -\frac{r^2}{4a_3}\,, \qquad (6)$$

$$E_0 = W_1(4\pi d t_1)^{p/2}\,\mathrm{e}^{a_1}\,.$$

Alternatively, we may also use

$$\eta_i = -\frac{a_2}{\beta_0}\,,$$

$$\eta_s = -\frac{4\beta_0 a_3}{p r^2}\,, \qquad (7)$$

$$E_0 = W_1\left(\frac{4\pi\beta_0 t_1}{p\eta_s}\right)^{p/2}\mathrm{e}^{a_1}\,.$$

One single seismogram can be inverted for the three parameters b, d and E_0 (or η_i, η_s and E_0). The early part of the seismogram, before the energy maximum, is sensitive to the diffusivity d (or η_s), whereas the late part following the maximum determines the coefficient of intrinsic attenuation b (or η_i). This indicates that the two parameters can be determined with only a small trade-off. The third parameter, E_0, has no influence on the waveform, only on the absolute value. It is used to account for the different site amplifications at the different seismometer sites. Since the diffusion model is an approximation for strong scattering, the mean free time should be much smaller than the observation time [$t \gg (\eta_s\beta_0)^{-1}$]. Therefore, near the source the model is valid only for the late part of the seismogram. To invert also for the diffusivity d (or η_s), however, we need the early part of the seismogram. For this reason we restrict the inversion to recordings with a minimum offset $r \geq 1$ km. We show that the mean free path η_s^{-1} is approximately 100 m (independent of frequency). For that reason, at a distance of $r \gg \eta_s^{-1} \approx 100$ m the whole seismogram is described by the diffusion model.

In the first step of processing we applied a Butterworth bandpass filter (forward–backward filtering, each of order 2) with centre frequencies of 4, 8, 12, 16 and 20 Hz using a constant bandwidth of 4 Hz (Fig. 6). At profile BEB, with the best data quality, we achieved results up to 20 Hz, whereas the seismograms of profile TRO, with the lowest signal-to-noise ratio, could be inverted only until 12 Hz. We then computed the energy density from the seismograms using the following equation:

$$W(\mathbf{r}, t) = \sum_{i=1}^{3} [f_i(\mathbf{r}, t)]^2 + [H\{f_i(\mathbf{r}, t)\}]^2\,, \qquad (8)$$

where $W(\mathbf{r}, t)$ is the (observed) energy density at location $\mathbf{r}$ and time t, $f_i(\mathbf{r}, t)$ is the bandpass-filtered seismogram (i-component) at location $\mathbf{r}$ and time t, and $H\{f\}$ is the Hilbert transformation of f. We tested a smoothing of the envelopes (Fig. 7), but omitted it for the final inversion. By taking the logarithm and multiplying by the geometrical factor $t^{p/2}$, we finally transform the observed data to the quantity $\ln[H(t)]$ of eq. (4) and compute the linear inversion. We estimate the S-wave velocity to be $\beta_0 = 1.4 \pm 0.3\ \mathrm{km\ s^{-1}}$ (see discussion below). Assuming the dominance of SS scattering and a constant value for β_0, we compute a theoretical S-wave arrival time using the equation $t_S = r/(1.4\ \mathrm{km\ s^{-1}})$. This time marks the start of the time window used for the inversion (Fig. 6). The P wave and the P coda are assumed to be outside this window. As can be seen in Fig. 6, almost all of the energy follows after the theoretical arrival time of the direct S wave. This is a good argument for the scalar approximation. The end of the inversion window corresponds to the time where the amplitude of the signal decreases below four times the noise level (Fig. 6). To invert

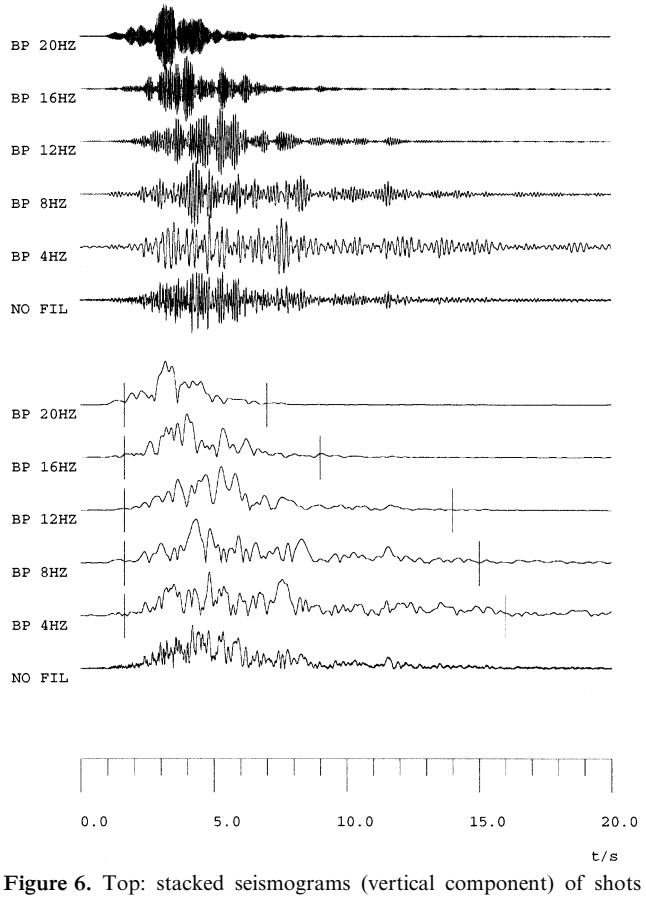

Figure 6. Top: stacked seismograms (vertical component) of shots from the source BEB recorded at station BEB23 at a distance of 2.293 km. The figure shows the unfiltered data as well as the seismograms after application of bandpass filters with centre frequencies of 4, 8, 12, 16 and 20 Hz. Bottom: same traces as top after computing the envelope. The window used for the inversion is also marked.

for the intrinsic attenuation b (or η_i) with sufficient accuracy, the amplitude of the energy maximum must be much larger than the amplitude at the end of the inversion window. We also chose a factor of 4. This means that the maximum amplitude must be 16 times larger than the noise level. Seismograms that did not fulfil this requirement due to a low signal-to-noise ratio were not admitted to the inversion.

At profile BEB we used 14 stations with an offset range of 1.229–3.135 km, at BAB 14 stations between 1.408 and 3.747 km offset and at BIB 5 stations between 0.991 and 2.865 km offset. Table 1 gives the number of inverted three-component seismograms per frequency range.

After the inversion using a single seismogram we compute the mean values of the attenuation coefficients as well as the

Table 1. Number of inverted seismograms per profile and per frequency.

	4 Hz	8 Hz	12 Hz	16 Hz	20 Hz
BEB	13	14	14	13	13
BAB	10	7	2	–	–
BIB	3	5	5	2	1

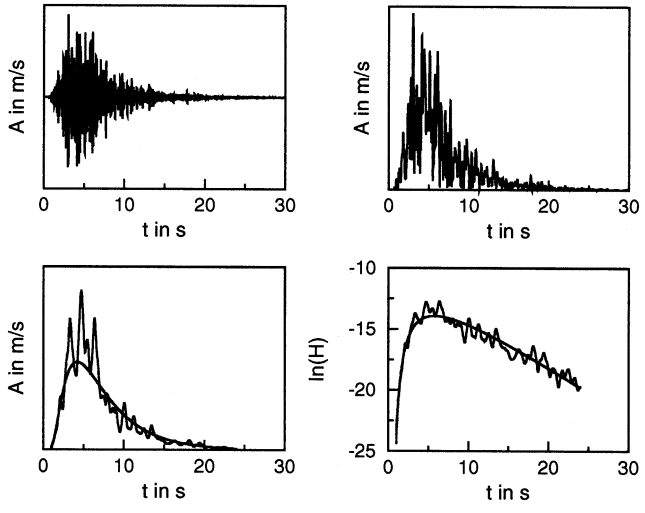

Figure 7. Steps of processing for the inversion using the diffusion model. The figure shows data from station BEB15, which is located at a distance of 1.396 km from the source BEB, as well as the best-fitting theoretical curve. Top left: bandpass-filtered vertical component (centre frequency 8 Hz); top right: envelope of seismogram; bottom left: envelope after smoothing with a 1 Hz low pass and control curve computed from the inversion result; bottom right: logarithmic representation used for linear inversion. Measured input curve as well as computed inversion result.

quality factors for each of the three profiles. The different values at different stations of one profile are used to estimate the error. This statistical error is a measure of the accuracy of the values of the attenuation coefficients. The scattering coefficient has a larger error of about 40 per cent, whereas the coefficient of intrinsic attenuation has an error of about 15 per cent. To estimate the inaccuracy of the frequency, we use the bandwidth of the bandpass filter of $\Delta f = 4$ Hz. Fig. 8 shows the mean values of the attenuation coefficients η_s and η_i for the three profiles BEB, BAB and BIB, including their error bounds. Additionally, all values, as well as the diffusivity and the quality factors Q, are given in Table 2, where we used the equations $Q_s = \omega/(\beta_0 \eta_s)$ and $Q_i = \omega/(\beta_0 \eta_i)$ to compute the quality factors.

The most important results are that at all examined frequencies the scattering coefficient is at least one order of magnitude larger than the coefficient of intrinsic attenuation ($\eta_s \gg \eta_i$). This means the attenuation of the direct wave is dominated by scattering attenuation, whereas intrinsic absorption can be neglected ($\eta = \eta_s + \eta_i \approx \eta_s$). Additionally, the mean free path η_s^{-1} is as low as 100 m. These two facts demonstrate that at Mt Merapi at a distance of a few hundred metres we move into the regime of strong scattering. The use of the diffusion model for an offset larger than 1 km as an approximation for strong scattering is consistent with the result of a mean free path of $\eta_s^{-1} = 100$ m. The strong scattering explains the observed seismograms, where the direct waves have very small amplitudes but the scattered waves carry almost all of the seismic energy. All three profiles show a similar frequency dependence of the attenuation coefficients. Using a double logarithmic scale we fitted two straight lines to the values of the coefficients for scattering and intrinsic attenuation at profile BEB with the best data quality. We obtain $\eta_s \sim f^{0.0}$ and $\eta_i \sim f^{1.6}$ (Fig. 8).

Table 2. Diffusivity d in km^2 s^{-1}, (temporal) coefficient of intrinsic attenuation b in s^{-1}, (spatial) coefficients of scattering attenuation η_s and intrinsic attenuation η_i in km^{-1} as well as the corresponding dimensionless quality factors Q_s and Q_i.

		04 Hz	08 Hz	12 Hz	16 Hz	20 Hz
	BEB	0.07±0.03	0.06±0.03	0.06±0.02	0.05±0.01	0.05±0.01
d	BAB	0.04±0.01	0.08±0.04	0.10±0.08	–	–
	BIB	0.03±0.01	0.06±0.03	0.05±0.03	0.04±0.02	–
	BEB	0.28±0.04	0.41±0.04	0.73±0.08	1.3±0.3	1.9±0.4
b	BAB	0.20±0.04	0.18±0.03	0.33±0.02	–	–
	BIB	0.35±0.06	0.44±0.02	0.8±0.2	1.5±0.1	–
	BEB	9±4	9±4	9±3	10±3	9±2
η_s	BAB	12±3	8±4	7±6	–	–
	BIB	14±2	11±6	12±7	14±7	–
	BEB	0.20±0.03	0.29±0.03	0.52±0.06	1.0±0.2	1.4±0.3
η_i	BAB	0.14±0.03	0.13±0.02	0.24±0.01	–	–
	BIB	0.25±0.04	0.31±0.01	0.61±0.15	1.1±0.11	–
	BEB	2.5±1.1	4.7±2.0	6.4±2.0	7.6±2.0	10.0±2.3
Q_s	BAB	1.6±0.4	5.9±3.4	10.9±8.8	–	–
	BIB	1.3±0.2	4.3±2.6	6.2±3.8	6.0±3.1	–
	BEB	93±14	123±11	104±12	78±14	69±15
Q_i	BAB	130±22	288±45	228±12	–	–
	BIB	73±13	115±5	93±18	68±7	–

4.2 Spatial variation of energy

In the last section we inverted each seismogram separately to derive the attenuation coefficients. The seismogram describes the variation of energy density in time. However, the diffusion model also predicts the variation of energy density in space (eq. 2). We use this fact to make a quantitative consistency check. Similar to the last section, we introduce the reference energy density W_1, where $W_1(r_1, t_1) = 1$ J m^{-3} for $t_1 = 1$ s, and take the logarithm. Eq. (2) then becomes

$$\ln\left[\frac{W(r)}{W_1}\right] = b_1 + b_2 r^2 , \tag{9}$$

with

$$b_1 = \ln\left[\frac{E_0}{W_1}\left(\frac{p\eta_s}{4\pi\beta_0 t}\right)^{p/2}\right] - \eta_i\beta_0 t , \tag{10}$$

$$b_2 = -\frac{p\eta_s}{4\beta_0 t} .$$

The logarithmic energy $\ln[W(r)]$ as a function of offset r depends linearly on the two base functions 1 and r^2. After the linear inversion for the two parameters b_1 and b_2 at a fixed time t we compute the scattering coefficient η_s using the following

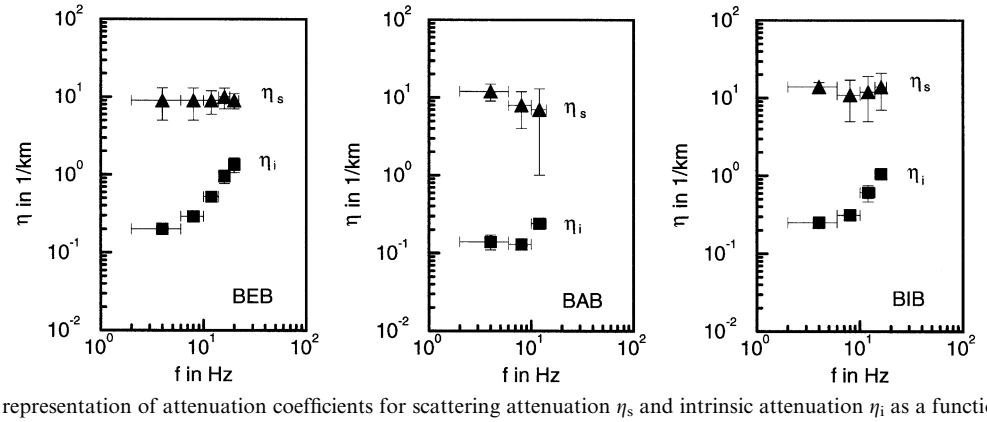

Figure 8. Log-log representation of attenuation coefficients for scattering attenuation η_s and intrinsic attenuation η_i as a function of frequency f at the three profiles BEB, BAB and BIB. The error bars correspond in the case of frequency to the bandwidth of the bandpass filter and in the case of attenuation coefficients to the statistical error.

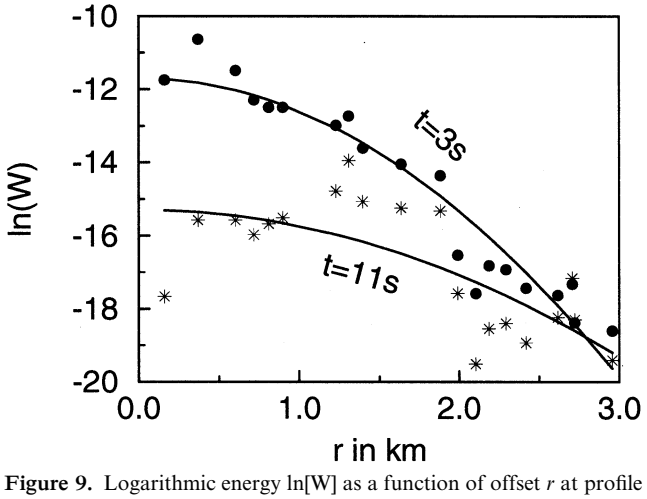

Figure 9. Logarithmic energy ln[W] as a function of offset r at profile BEB for the frequency band of 8 Hz using a time window width of 2 s. Circles correspond to the time window around 3 s (early coda, 2–4 s) and stars correspond to the time window around 11 s (late coda, 10–12 s). The two lines are the best-fitting model curves assuming a parabolic decay of logarithmic energy as predicted by the diffusion model.

equation:

$$\eta_s = -\frac{4\beta_0 t b_2}{p}.$$

Applying the same procedure as in the last section we compute the envelopes of the seismograms for the centre frequencies 4, 8 and 12 Hz at BEB, the profile with the best data quality. We then compute the mean values of the logarithmic energy within the time windows 2–4, 4–6, 6–8, 8–10, 10–12, 12–14 and 14–16 s. These values as a function of offset are plotted separately for each time window. We do not apply any corrections for possible different site amplifications. Fig. 9 shows an example for the time windows 2–4 and 10–12 s using the 8 Hz bandpass filter. At 4 and 12 Hz the behaviour is similar. For the higher frequencies (16 and 20 Hz), due to the faster temporal decay of the coda we cannot use the late time windows (*cf.* Fig. 6). In the early coda most of the energy is spatially concentrated near the seismic source. For later time windows the energy is distributed more and more homogeneously. This spatial behaviour is typical of diffusion. Fitting parabolic curves to the data, we invert for the scattering coefficient η_s in the spatial domain. For each time window we obtain an independent value of η_s. Again we compute the mean value and estimate the error using the statistical variance. Table 3 shows a comparison of the values of η_s obtained from the two independent inversions using the temporal variation of energy and the spatial variation of energy. Within their error bounds both methods have the same result.

Table 3. Coefficients of scattering attenuation η_s in km^{-1} for profile BEB derived from the temporal variation of energy as well as from the spatial variation of energy.

	4 Hz	8 Hz	12 Hz
$\eta_{s,\,time}$	9 ± 4	9 ± 4	9 ± 3
$\eta_{s,\,space}$	9 ± 3	7 ± 3	7 ± 2

4.3 Energy maximum

The largest amplitudes in the seismogram will be the last ones to fall below the noise level. At large distances we may observe only this part of the whole signal, and therefore we want to study it in more detail.

First we compute the arrival time t_{max} of the energy maximum, which must fulfil the following equation:

$$\frac{\partial W}{\partial t} = 0 \qquad \text{for} \qquad t = t_{max}\,. \tag{12}$$

Eq. (2) is differentiated with respect to time and equated to zero. We obtain

$$t_{max} = \frac{1}{\beta_0}\sqrt{\frac{3}{4\eta_i}\left(\frac{3}{4\eta_i} + \eta_s r^2\right)} - \frac{3}{4\beta_0\eta_i}\,. \tag{13}$$

Estimating $\eta_i \approx 0.5$ km^{-1} and $\eta_s \approx 10$ km^{-1}, the term depending on distance r is much larger than the others, if $r \geq 1$ km. Therefore, we can use the same approximation as Dainty & Toksöz (1981) did for the moon,

$$t_{max} \approx \frac{r}{\beta_0}\sqrt{\frac{3\eta_s}{4\eta_i}} \qquad \text{for} \qquad r \geq 1 \text{ km}\,. \tag{14}$$

The group velocity U of the transport of energy around the maximum of the envelope can be computed from

$$U = \left.\frac{dr}{dt}\right|_{W=W_{max}} = \frac{1}{\dfrac{dt_{max}}{dr}} = \beta_0\sqrt{\frac{4\eta_i}{3\eta_s}}. \tag{15}$$

Using the values for η_i and η_s of Table 2 we obtain $U \approx 200$–300 m s^{-1} for the 8 Hz bandpass, which is of the order of the observed propagation velocity. The corresponding value of the energy density $W(r, t_{max})$ is

$$W(r, t_{max}) = E_0\left(\frac{3\eta_i\eta_s}{4\pi^2 r^2}\right)^{3/4}\exp(-r\sqrt{3\eta_i\eta_s})\,. \tag{16}$$

This means that the energy density decays exponentially multiplied by a geometrical factor of $r^{-3/2}$. Using the reference energy density W_1 and the reference distance r_1, we conclude that

$$\ln(H) = \ln\left(\frac{W}{W_1}\right) + \frac{3}{2}\ln\left(\frac{r}{r_1}\right) = -\eta_{max}(r - r_0)\,, \tag{17}$$

where we have introduced the attenuation coefficient $\eta_{max} = \sqrt{3\eta_i\eta_s}$ for the energy maximum. To compare this with the data, we measure the maximum amplitude occurring in each seismogram at profile BEB. Fig. 10 shows the logarithm of the energy corrected for the geometrical factor $r^{3/2}$ as a function of offset r. The slope of the fitted straight line corresponds to the attenuation coefficient η_{max} of the energy maximum. Using the main frequency band around 8 Hz we compare the measured values with the predictions of the diffusion model (Table 4). The values of η_i and η_s used to compute $\eta_{max} = \sqrt{3\eta_i\eta_s}$ are inverted from the temporal variation of energy density only (Table 2). Both values of η_{max} are in agreement with each other (Table 4). This is another proof that the diffusion model explains the temporal as well as the spatial properties of the energy density using the same values for the parameters η_i and η_s.

Table 4. Comparison of two values for the coefficient η_{max} of attenuation of the energy maximum at profiles BEB and BAB in km^{-1} ($f=8$ Hz). Column 1: attenuation derived from measuring the amplitudes of the energy maximum as a function of offset. Column 2: attenuation derived from temporal variation of energy (envelopes of seismograms) and using the equation $\eta_{max}=\sqrt{3\eta_i\eta_s}$.

Profile	Measured values	Diffusion model
BEB	2.4 ± 0.2	2.8 ± 0.8
BAB	1.6 ± 0.2	1.8 ± 0.6

4.4 Limitations

The diffusion model is a very simplified model. Therefore, we discuss here its limitations and major problems.

First, it assumes strong scattering. This means the distance between source and seismometer should be much larger than the mean free path ($r \gg \eta_s^{-1}$). We only used data from seismometers in an offset range larger than $r=1$ km, whereas the calculated mean free path is as low as $\eta_s^{-1}=100$ m. For that reason, the approximation of strong scattering is self-consistent and useful.

The energy transport theory assumes point-like scatterers. Therefore, the mean free path η_s^{-1} should be much larger than the wavelength λ of the seismic waves. If the mean free path and the wavelength are of comparable size, the diffusion model may fail, and a more complicated interaction of the wavefield with the medium may take place. This effect, called 'Anderson localization' (Anderson 1958), can completely block the propagation of waves at a certain frequency. The easiest definition of this phenomena is that the apparent mean free path η_s^{-1} approaches zero for this frequency range (Van Tiggelen 1999). A generally accepted approximate criterion for the localization of waves in 3-D random media is the so-called 'Ioffe–Regel criterion'. This criterion states that the diffusion model is no longer valid but Anderson localization occurs if the wavelength λ of the seismic wave is larger than 2π times the mean free path η_s^{-1} (Van Tiggelen 1999),

$$\lambda > 2\pi\,\eta_s^{-1}\,. \tag{18}$$

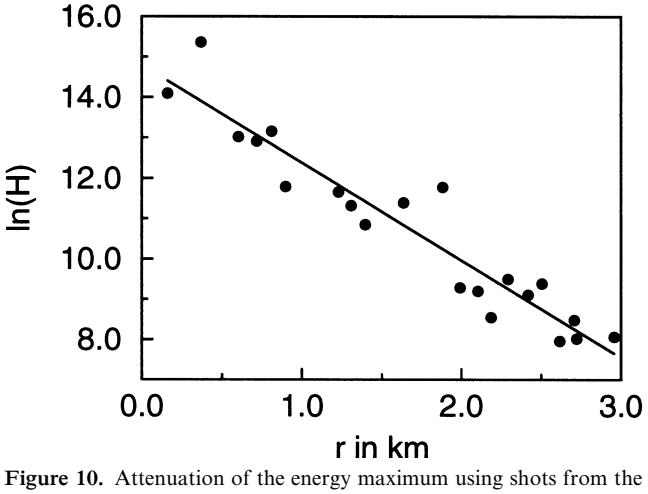

Figure 10. Attenuation of the energy maximum using shots from the source BEB recorded at profile BEB. The line is the best fit assuming $W(r,\,t_{max})\sim r^{-3/2}\,e^{-\eta_{max}r}$ as predicted by the diffusion model.

Recently, Anderson localization was discussed for Piton de la Fournaise volcano by Aki & Ferrazzini (2000). Weaver (1990) reported an observation of Anderson localization in laboratory experiments using ultrasound. According to this author the distribution of energy will show the following characteristics different from the diffusion model:

(i) for late times the energy is not homogeneously distributed in space but still localized near the source;
(ii) the apparent mean free path η_s^{-1} using the diffusion model depends on the frequency approaching zero values near the regime of Anderson localization;
(iii) the observed scattering coefficient η_s using the diffusion model seems to increase with distance.

At Merapi volcano we used frequencies between 4 and 20 Hz. Assuming an *S*-wave velocity of 1.4 km s^{-1}, this corresponds to wavelengths between 70 and 350 m. Using the derived mean free path of 100 m, Anderson localization will occur at a wavelength around 600 m, corresponding to a frequency of around 2 Hz. However, although we approached the regime of localization, we did not observe any of the effects reported by Weaver (1990). At late time windows the spatial distribution of energy is not localized, but approaches a constant value, as expected for the diffusion model (Fig. 9). Additionally the scattering coefficient is independent of frequency (Fig. 8) and does not increase with distance. In fact, it decreases with distance, as discussed below. Therefore, we found the diffusion model still to be reliable, although the wavelength is of the same order as the mean free path.

Next we assume that coda consists mainly of *S*-to-*S* scattered waves, neglecting *P* and surface waves. The ratio of *P*- and *S*-wave energy in the coda is determined by the conversion scattering coefficients η_s^{PS} and η_s^{SP}. The Born approximation predicts (Sato & Fehler 1998, p. 105)

$$\eta_s^{PS} = 2\,\frac{\alpha_0^2}{\beta_0^2}\,\eta_s^{SP}\,. \tag{19}$$

Since the *P*-wave velocity α_0 is always larger than the *S*-wave velocity β_0, *P* waves convert faster into *S* waves than the other way round. Aki (1992) demonstrated that this is generally valid and therefore also holds for strong scattering. After the occurrence of many scattering processes, the ratio of *P* to *S* waves approaches its equilibrium state, which is determined by eq. (19) only and is independent of the original source. For this reason we theoretically have to expect the dominance of *S* waves over *P* waves at large distances $[r \gg (\eta_s^{PS})^{-1}]$. At Merapi we found a dominance of the horizontal components. This can be interpreted as *S* waves arriving almost vertically due to the near-surface low-velocity layer. Therefore, the assumption of a dominance of *S* waves over *P* waves is reasonable. The effect of surface waves, however, is more difficult to estimate and is discussed below.

Another simplification of the diffusion model is the assumption of isotropic scattering. For weak scattering this is never valid (Wu & Aki 1985). In the case of Rayleigh or Mie scattering these authors found wide-angle scattering strongly depending on the scattering angle and strong forward scattering in the case of small wavelength. For strong scattering, however, this problem simplifies. Using the Monte Carlo simulation, Gusev & Abubakirov (1996) showed that the strong multiple scattering process is always isotropic. Following these authors, the effective scattering coefficient for multiple scattering is

determined by the following equation:

$$\eta_{s,eff} = \eta_{s,0} - \int \cos\vartheta\, \eta_s(\varphi, \vartheta)\, d\Omega, \quad (20)$$

where $\eta_s(\varphi, \vartheta)$ is the angle-dependent scattering coefficient and $\eta_{s,0}$ the total scattering coefficient of the single scattering process. In the strong scattering regime ($r \gg \eta_{s,eff}^{-1}$), the underlying angular dependence of the scattering coefficient of the single scattering process is no longer important; only the effective scattering coefficient $\eta_{s,eff}$ controls the measured seismograms. Therefore, the diffusion model can be applied, even if the single scattering process is dominated by forward scattering. In that case, however, in the inversion procedure we measure the effective scattering coefficient $\eta_{s,eff}$ describing the scattering process. This effective scattering coefficient is no longer identical to the true scattering coefficient $\eta_{s,0}$ describing the damping of the direct *S* wave. For details see Ishimaru (1978, pp. 175–178) and Gusev & Abubakirov (1996). Similar to eq. (20), Sato & Fehler (1998, p. 125) used

$$\eta_{s,eff} = \int H(\vartheta - \vartheta_0)\, \eta_s(\varphi, \vartheta)\, d\Omega \quad (21)$$

to calculate a traveltime-corrected Born approximation, where H is the Heaviside function and ϑ_0 is a cut-off angle to exclude forward scattering. Following these authors and assuming an exponential autocorrelation function, the frequency independence of the scattering coefficient indicates that the correlation length a of the medium is larger than the wavelengths used in the experiment. This means that the single scattering process is indeed dominated by forward scattering. A frequency independence of the scattering coefficient η_s is also consistent with observations in many other regions of the world (e.g. Sato & Fehler 1998, pp. 55 and 110).

Applying the diffusion model, we have to assume a spatial constant value of the diffusivity d. Since $d = \beta_0 \eta_s^{-1}/3$, this also means a constant value of the background *S*-wave velocity β_0. There are two problems: first we know that β_0 is not constant, but increases with depth, and second it is impossible to derive the value of the *S*-wave velocity from the direct *S* wave. Due to the strong scattering the direct *S* wave is attenuated quickly and additionally superimposed by the *P* coda. However, we can use the first onsets of the seismograms to measure the *P*-wave velocity. In the distance range of 1–3 km used in this analysis, we find a corresponding *P*-wave velocity of around 2.8–3.0 km s^{-1}. Estimating the *S*-wave velocity as half of the *P*-wave velocity, we obtain $\beta_0 \approx 1.4$ km s^{-1}. We assume an error as large as $\Delta\beta_0 = 0.3$ km s^{-1} for this estimation, so the smallest value ($\beta_0 = 1.1$ km s^{-1}) corresponds to an α_0/β_0 ratio of 2.6 and the largest value ($\beta_0 = 1.7$ km s^{-1}) corresponds to an α_0/β_0 ratio of 1.7. For more details on the analysis of direct waves see Wegler (1999, pp. 25–37). The estimation of β_0 influences our inversion at two different steps: first we use it to select the inversion window, which starts at the theoretical *S*-wave arrival time, and second we use it to convert the diffusivity d and the (temporal) coefficient of intrinsic attenuation b to the coefficient of scattering and intrinsic attenuation η_s and η_i (eq. 3). To check the dependence on the *S*-wave velocity, we inverted profile BEB again using the extreme values of $\beta_0 = 1.1$ km s^{-1} and $\beta_0 = 1.7$ km s^{-1} instead of $\beta_0 = 1.4$ km s^{-1}. Table 5 shows the results for the three different *S* velocities assumed. The values of the diffusivity d and the (temporal) coefficient of intrinsic attenuation b are almost independent of our choice of the *S*-wave velocity. This means that the small shift of the start time of the inversion window does not significantly influence the results. On the other hand, the attenuation coefficients η_s and η_i change by up to 30 per cent. For the coefficient of scattering attenuation η_s, this systematic error due to the uncertainty in background *S*-wave velocity is still smaller than the statistical error due to the variance of this value at different stations. For the coefficient of intrinsic attenuation η_i, the systematic error is more important than the statistical error.

The last two assumptions we want to discuss here are the assumption of a spatially constant *S*-wave velocity β_0 and the assumption of a spatially constant scattering coefficient η_s. We will show that these two assumptions are the most problematic. In particular, the depth dependence of these two values should be accounted for in later, more detailed investigations.

Measuring the first onset of *P* waves, Lühr *et al.* (1998) and Wegler (1999, pp. 25–31) found low values of *P*-wave velocity in the shallow subsurface layers along the same profiles as

Table 5. Dependence of the inversion result for the diffusivity d (in km^2 s^{-1}), the (temporal) coefficient of intrinsic attenuation b (in s^{-1}) and the damping coefficients η_s and η_i (in km^{-1}) on the value of the background velocity β_0 (in km s^{-1}) of *S* waves using the example of profile BEB.

	β_0	04 Hz	08 Hz	12 Hz	16 Hz	20 Hz
	1.1	0.26±0.05	0.41±0.04	0.74±0.09	1.4±0.3	2.1±0.5
b	1.4	0.28±0.04	0.41±0.04	0.73±0.08	1.3±0.3	1.9±0.4
	1.7	0.27±0.04	0.40±0.04	0.70±0.08	1.2±0.3	1.7±0.3
	1.1	0.07±0.04	0.06±0.03	0.05±0.02	0.05±0.01	0.04±0.01
d	1.4	0.07±0.03	0.06±0.03	0.06±0.02	0.05±0.01	0.05±0.01
	1.7	0.07±0.03	0.06±0.03	0.06±0.02	0.06±0.02	0.06±0.02
	1.1	0.23±0.05	0.37±0.04	0.68±0.08	1.3±0.3	1.9±0.4
η_i	1.4	0.20±0.03	0.29±0.03	0.52±0.06	1.0±0.2	1.4±0.3
	1.7	0.16±0.02	0.24±0.02	0.41±0.05	0.7±0.2	1.0±0.2
	1.1	6±4	7±3	8±3	9±2	9±2
η_s	1.4	9±4	9±4	9±3	10±3	9±2
	1.7	10±4	11±5	11±4	11±3	11±3

discussed here. Therefore, it is reasonable to assume also a depth-dependent background *S*-wave velocity, but the diffusion model does not take into account this evidence. Since the artificial sources are located at the Earth's surface, which is within the low-velocity layer, the energy is captured in this waveguide. This may produce strong surface waves and resonance effects. Could such surface waves be the dominant feature and explain the observed seismograms equally as well as the diffusion model? The dispersion properties may cause a delay of the energy maximum and the arrival of different modes of Love and Rayleigh waves may cause the observed incoherence and the complicated polarization properties. However, weakly scattered surface waves cannot explain the spatial variation of energy; there is a clear concentration of energy near the source location (Fig. 9). This spatial distribution of energy is characteristic of diffusion, whereas weakly scattered surface waves propagate with a certain velocity away from the source. Fig. 9 excludes weakly scattered surface waves but not strongly scattered surface waves. We discuss the possibility of diffusive surface waves instead of diffusive body waves below.

The derived value for the mean free path of around 100 m is extremely low. If we assume that the propagation medium slowly changes with depth into the usual Earth's crust, the scattering coefficient has to be strongly depth-dependent. In the subsurface layers there may be very strong impedance contrasts such as areas with fine ash bordering massive blocks. With increasing time and depth, however, these contrasts will decrease, causing a depth-dependent scattering coefficient. The similar problem of a depth-dependent scattering coefficient appears on the moon. Dainty & Toksöz (1981) reported that on the moon the delay time between the direct *S* wave and the energy maximum, starting at a certain critical distance from the source, no longer increases. The observed envelope for larger distances stays almost constant. For this reason Nakamura (1977) found, using the diffusion model, that the inverted scattering coefficient seems to decreases with distance. Additionally, deep moonquakes show a short delay time that is less scattering than near-surface ones show. These observations were interpreted such that only the upper layers of the moon are strongly scattering, whereas the seismic waves can propagate almost undisturbed in deeper areas. For details see Dainty & Toksöz (1981). The propagation medium at Merapi volcano shows similar characteristics. Using the diffusion model with a homogeneous distribution of scatterers, we obtain a scattering coefficient decreasing with distance. Fig. 11 shows this effect for the 8 Hz bandpass at profile BEB. The attenuation coefficients computed using envelopes of seismograms are shown as a function of the distance between receiver and source locations. (Fig. 8, in contrast, shows the mean values for the distance range 1–4 km. The large statistical error for the scattering coefficient in this figure is caused by the variance with distance and can probably be reduced significantly by applying models with depth-dependent scattering coefficients.) Fig. 11 additionally shows the formal inversion results for the near-source seismometers at an offset range of 162 m to 1 km and for shots recorded at the mini-array GRW on the opposite flank of the volcano ($r \approx 7$ km). These values were not used in the computation of mean values. Another observation supporting the idea of depth-dependent scattering is the volcanic earthquakes. Ratdomopurbo (1995, pp. 25–37) distinguished A- and B-type events. Following this author, the A-type events occur at a depth of greater than 2 km below the summit. These deep events show clear *P* as well as

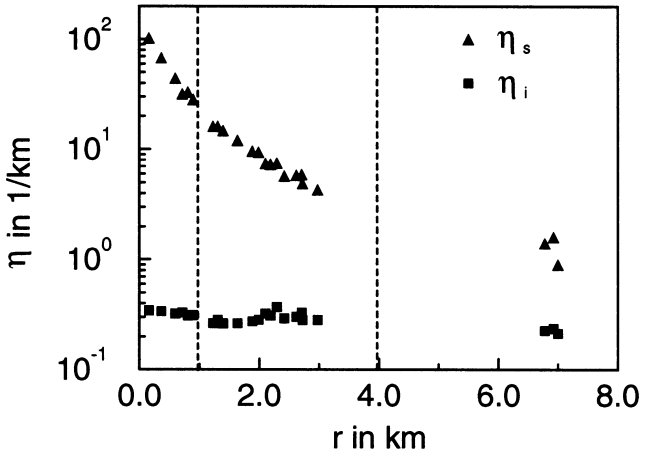

Figure 11. Dependence of the attenuation coefficients η_s and η_i on the distance r between source and receiver using the 8 Hz bandpass and shots from the source BEB. The inversion was performed using envelopes of seismograms (temporal variation of energy). The window from almost 1 to 4 km marked with dotted lines is used for computing the mean values of profile BEB shown in Fig. 8. In addition, the figure shows the inversion results for recordings at the opposite flank of the volcano (array GRW) as well as for the near-source recordings of profile BEB.

S phases, whereas the B-type events are shallow and show no *S* phase. This can be explained if the deep events mainly propagate through weakly scattering material and only cross the strong scattering layer near the seismometer, whereas the signals of shallow events are scattered near the source as well as near the seismometer.

If the scattering coefficient is much larger near the surface, we can also understand why the low-velocity layer is not acting as a waveguide. Within the near- surface low-velocity layer, the inhomogeneities are the strongest, causing a fast decrease of energy. Therefore, at large distances the energy propagating in deeper regions dominates. We found some hints for a depth-dependent scattering coefficient. Therefore, the use of a homogeneous distribution of scatterers in the diffusion model is one of its major shortcomings. The second problem is the increase of *S*-wave velocity with depth, and in particular the near-surface low-velocity layer, which may cause significant surface waves, whereas we assumed pure *S* waves. However, we found a scattering coefficient decreasing with distance, which corresponds to a diffusivity increasing with distance. This might be explained within the body wave model by a depth-dependent scattering coefficient. If we assume diffusive surface waves, we also obtain a spatial variance of the diffusivity similar to Fig. 11, but we cannot explain this observation in the surface wave model. From Fig. 11 we suggest that the dominant feature is scattered body waves, whereas the surface waves cause only secondary effects.

5 DISCUSSION

Using envelopes of bandpass-filtered seismograms and the diffusion model we derived a mean free path of the order of 100 m for the shallow structure of Merapi volcano in the frequency range 4–20 Hz. In the time domain each seismogram can be inverted for separately, where the attenuation coefficients

are computed from the shape of the envelope only. Therefore, the site amplification factor at different seismometer locations has no influence on the inversion results. Neglecting the site amplification problem we measured the spatial decay of energy in different time windows. Using this independent method we could reconfirm our main result of the time-domain inversion ($\eta_s^{-1} \approx 100$ m).

This value is extremely low compared to that of the usual material of the Earth's crust (e.g. Sato & Fehler 1998, p. 55) or other results in volcanic regions (Mayeda *et al.* 1992; Londoño 1996). However, we note that our experiment concentrates on the shallow structure within a radius of 5 km around the active summit, whereas the studies mentioned above image a much larger and deeper region. The strong scattering at Merapi corresponds to strong inhomogeneities observable at the surface. The volcanic edifice consists of alternating deposits of pyroclastic flows, lahars, ash falls and lava flows (Gertisser & Keller 1998; Schwarzkopf *et al.* 1998). The irregular topography of the surface due to erosion causes a strong lateral variation of deposition. We expect strong 3-D variations in density and *P*- and *S*-wave velocities that may cause the observed strong scattering.

Assuming strong scattering, many of the characteristics of the observed seismograms can be explained. The waveform of the envelopes can be modelled by the diffusion model. In this model the slow increase of energy to a maximum following the direct waves is explained by multiple scattered waves. The exponential decay of energy in the very late part of the seismogram, in contrast, is not unusual and can be expected for weak as well as for strong scattering. The most important argument for the diffusion model is the spatial distribution of energy, which for all times shows a concentration of energy near the source location. Additionally, strong scattering can explain the coherence and polarization properties. The *P* wave is the only phase in a classic sense. Therefore, it is coherent over the seismometer spacing used. All other energy, in contrast, is a superposition of scattered waves and arrives mainly as incoherent energy. Moreover, the scattered waves arrive from all azimuths and cause an almost arbitrary polarization azimuth. The slight dominance of the horizontal components is more difficult to understand. One possible explanation is the observed near-surface low-velocity layer, where the *P*-wave velocity increases from about $\alpha_0 = 0.8$ to 2.8 km s^{-1} within the first 200 m depth (Lühr *et al.* 1998; Wegler 1999, pp. 25–31). Since the scattered waves are mainly *S* waves arriving almost vertically due to the low-velocity layer, most of the energy will be on the horizontal components.

The major problem of our model is that we assume a spatial homogeneous scattering coefficient η_s (or diffusivity d). This is in contradiction to Fig. 11, which shows a systematic decrease of the scattering coefficient η_s with increasing distance r. We think that in a future, more detailed model this problem can be solved by introducing a scattering coefficient $\eta_s(z)$ decreasing with depth. Such a depth-dependent model requires the assumption of body waves. The seismograms observed at greater distances are dominated by energy that has travelled through the more homogeneous deeper material. This will cause an apparent decrease of the scattering coefficient η_s with increasing source–receiver distance, as observed in Fig. 11. On the other hand, we may assume diffusive surface waves instead of diffusive body waves. Such a surface wave model can explain the data equally well within the homogeneous diffusion model

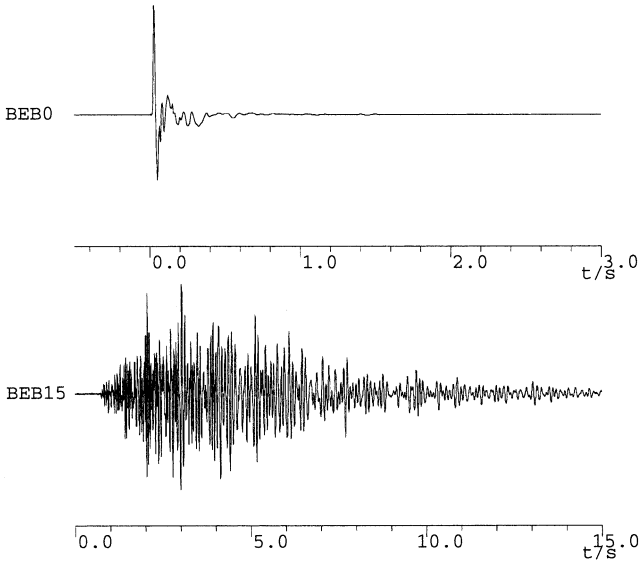

Figure 12. Top: seismogram of the artificial source in BEB (vertical component) recorded at a distance of 4 m. Bottom: seismogram of the artificial source in BEB (vertical component) recorded at a distance of 1.396 km.

(eq. 2 with $p = 2$). However, in the surface wave model we also obtain a scattering coefficient η_s decreasing with increasing source–receiver distance similar to Fig. 11. This problem can be solved within the body wave model by the quite realistic assumption of a depth-dependent diffusivity, but cannot be solved within the surface wave model. Therefore, Fig. 11 strongly suggests the use of diffusive body waves instead of diffusive surface waves.

For the natural seismic events, multiple scattering is also one of the major physical processes causing the observed seismograms. As an example, Figs 12 and 13 show the signals of a shot and of a natural volcanic event. This event would be classified in the categories of Minakami (1960) as a B-type event. Ratdomopurbo (1995, pp. 25–37) calls this class of events volcanotectonic type B to distinguish them from multiple-phase and long-period events. The frequency content of this class of signals is comparable to that of volcanotectonic events of type A (Ratdomopurbo 1995, pp. 27 and 38–39). Concerning the interpretation of such B-type events, the classic methods of seismology face the following problems.

(i) There are no distinct phases, but the energy increases and decreases smoothly. Only large events show a small *P* onset. *S* onsets are almost never observed.

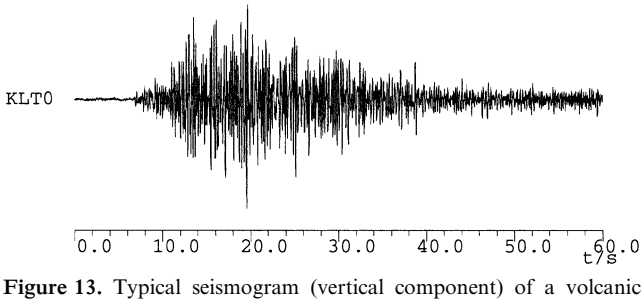

Figure 13. Typical seismogram (vertical component) of a volcanic B-type event recorded at station KLT0 at a distance of around 2 km from the active dome.

(ii) There is no coherence over usual station distances.

(iii) The polarization changes quickly in time showing no preferred azimuth.

In our interpretation the signals of shallow natural volcanic events are like the shots strongly influenced by scattering effects. We suspect that these B-type events have in fact the same simple impulsive source process as A-type events. The difference in the observed seismograms is caused by the different propagation path, where the deep A-type events mainly propagate through weakly scattering material and the shallow B-type events propagate through the strongly scattering shallow structure of the volcanic edifice. At Merapi this idea is supported by the fact that volcanotectonic A-type events are deep and volcanotectonic B-type events are shallow (Ratdomopurbo 1995, pp. 70–77). Since the original work of Minakami (1960) it is a well-known fact that at other volcanoes also B-type events usually occur at shallow depths, whereas A-type events originate from deep sources. This indicates that the concept of multiple scattering might be useful at other volcanoes also. Following this interpretation, the seismogram of volcanotectonic B-type events consists of only two parts: a small *P* onset followed by the slowly increasing spindle-like coda. Since the coda waves have an amplitude about 20 times larger than the *P* onset, at larger distances the whole seismogram consists of coda without any classic phase. How can we deal with such signals? If there is a small *P* onset, we can apply classic methods. We can make use of the following two characteristics to detect the *P* onset: first, due to the low-velocity layer it should have vertical polarization, whereas multiple scattered noise and coda waves are *S* waves and show horizontal polarization, and second, the *P* onset as a classic phase arrives as a coherent wave, whereas the coda is mainly incoherent. Therefore, mini-arrays as used at Merapi volcano by Wassermann *et al.* (1999) are very helpful in detecting the coherent *P* wave. At larger distances, when the small *P* onset is already below the noise level, we observe only coda waves and classic methods will fail. Following Sato & Fehler (1998, pp. 197–203), the original source radiation pattern will converge to spherical symmetry in the late coda. Therefore, we cannot extract the complete source function from the coda. However, in principle, using eq. (2) we may invert the signals for the source spectrum, and even for source time and location, if the parameters of the propagation medium are well known.

ACKNOWLEDGMENTS

We would like to thank the Volcanological Technology Research Center (BPPTK), Yogyakarta, for the logistical support, and the students of the FMIPA, Universitas Gadjah Mada Sekip Unit III, Yogyakarta, for their enthusiastic efforts during the field campaign. Three airguns were made available by Alfred-Wegener-Institut (AWI), Bremerhaven, and the seismic equipment by the Geophysical Instrument Pool, Potsdam (GIPP). We used the free GMT software of P. Wessel and W. H. F. Smith as well as Seismic Handler of K. Stammler. The study was financially supported by the Deutsche Forschungsgemeinschaft (DFG) and the GeoForschungsZentrum Potsdam (GFZ). We would also like to thank F. Krüger and H. Sato for their suggestions on the manuscript. The helpful reviews of J. Neuberg and an anonymous reviewer further improved this article.

REFERENCES

Aki, K., 1992. Scattering conversions P to S versus S to P, *Bull. seism. Soc. Am.,* **82,** 1969–1972.

Aki, K. & Chouet, B., 1975. Origin of coda waves: source, attenuation, and scattering effects, *J. geophys. Res.,* **80,** 3322–3342.

Aki, K. & Ferrazzini, V., 2000. Seismic monitoring and modeling of an active volcano for prediction, *J. geophys. Res.,* **105,** 16 617–16 640.

Anderson, P.W., 1958. Absense of diffusion in certain random lattice, *Phys. Rev.,* **109,** 1492–1505.

Dainty, A M. & Toksöz, M.N., 1977. Elastic wave propagation in a highly scattering medium—a diffusion approach, *J. Geophys.,* **43,** 375–388.

Dainty, A.M. & Toksöz, M.N., 1981. Seismic codas on the earth and the moon: a comparison, *Phys. Earth planet. Inter.,* **26,** 250–260.

Del Pezzo, E., Ibanez, J., Morales, J., Akinci, A. & Maresca, R., 1995. Measurements of intrinsic and scattering seismic attenuation in the crust, *Bull. seism. Soc. Am.,* **85,** 1373–1380.

Del Pezzo, E., Simini, M. & Ibañez, J.M., 1996. Separation of intrinsic and scattering Q for volcanic areas: a comparison between Etna and Campi Flegrei, *J. Volc. Geotherm. Res.,* **70,** 213–219.

Evans, J.R. & Zucca, J.J., 1988. Active high-resolution seismic tomography of compressional wave velocity and attenuation structure at Medicine Lake volcano, northern California Cascade Range, *J. geophys. Res.,* **93,** 15 016–15 036.

Fehler, M., Roberts, P. & Fairbanks, T., 1988. A temporal change in coda wave attenuation observed during an eruption of Mount St. Helens, *J. geophys. Res.,* **93,** 4367–4373.

Fehler, M., Hoshiba, M., Sato, H. & Obara, K., 1992. Separation of scattering and intrinsic attenuation for the Kanto-Tokai region, Japan, using measurements of S-wave energy versus hypocentral distance, *Geophys. J. Int.,* **108,** 787–800.

Gertisser, R. & Keller, J., 1998. The holocene volcanic activity and magmatic evolution of Merapi volcano, central Java: constraints from stratigraphic, chronologic and geochemical data, in *Decade-Volcanoes under Investigation,* Vol. Sonderband III/1998 of DGG-Mitteilungen, pp. 15–19, eds Zschau, J. & Westerhaus, M., Deutsche Geophysikalische Gesellschaft.

Gusev, A.A. & Abubakirov, I.R., 1987. Monte-Carlo simulation of record envelope of a near earthquake, *Phys. Earth planet. Inter.,* **49,** 30–36.

Gusev, A.A. & Abubakirov, I.R., 1996. Simulated envelopes of non-isotropically scattered body waves as compared to observed ones: another manifestation of fractal heterogeneity, *Geophys. J. Int.,* **127,** 49–60.

Hoshiba, M., 1991. Simulation of multiple-scattered coda wave excitation based on the energy conservation law, *Phys. Earth planet. Inter.,* **67,** 123–136.

Ishimaru, A., 1978. *Wave Propagation and Scattering in Random Media,* Vol. I, Academic Press, New York.

Londoño, J.M., 1996. Temporal change in coda Q at Nevado Del Ruiz volcano, Colombia, *J. Volc. Geotherm. Res.,* **73,** 129–139.

Lühr, B.-G., Maerklin, N., Rabbel, W. & Wegler, U., 1998. Active seismic measurements at the Merapi volcano, Java, Indonesia, in *Decade-Volcanoes under Investigation,* Vol. Sonderband III/1998 of DGG-Mitteilungen, pp. 53–55, eds Zschau, J. & Westerhaus, M., Deutsche Geophysikalische Gesellschaft.

Mayeda, K., Koyanagi, S., Hoshiba, M., Aki, K. & Zeng, Y., 1992. A comparative study of scattering, intrinsic, and coda Q^{-1} for Hawaii, Long Valley Caldera, and central California between 1.5 and 15.0 hz, *J. geophys. Res.,* **97,** 6643–6659.

Minakami, T., 1960. Fundamental research for predicting volcanic eruptions (part 1) earthquakes and crustal deformations originating from volcanic activities, *Bull. Earthq. Res. Inst.,* **38,** 497–544.

Mori, J., 1995. Volcano seismology, hazard assessment, *Rev. Geophys.,* **33,** 263–267.

Nakamura, Y., 1977. Seismic energy transmission in an intensively scattering medium, *J. Geophys.,* **43,** 389–399.

Newhall, C., Fink, J., Decker, B., De La Cruz, S. & Wagner, J.-J., 1994. Research at Decade Volcanoes aimed at disaster prevention, *EOS, Trans. Am. geophys. Un.,* **75,** 340, 350.

Nishimura, T., Fehler, M., Baldridge, W.S., Roberts, P. & Steck, L., 1997. Heterogeneous structure around the Jemez volcanic field, New Mexico, USA, as inferred from the envelope inversion of active-experiment seismic data, *Geophys. J. Int.,* **131,** 667–681.

Ohrnberger, M., Wassermann, J. & Scherbaum, F., 1999. Detection and classification of seismic signals of volcanic origin at Mt. Merapi, Java, Indonesia, in *IUGG Abstracts,* vol. B, p. 156, Birmingham.

Patanè, D., Ferrucci, F. & Gresta, S., 1994. Spectral features of microearthquakes in volcanic areas: attenuation in the crust and amplitude response of the site at Mt. Etna, Italy, *Bull. seism. Soc. Am.,* **84,** 1842–1860.

Press, W.H., Flannery, B.P., Teukolsky, S.A. & Vetterling, W.T., 1988. *Numerical Recipes in C: the Art of Scientific Computing,* Cambridge University Press, Cambridge.

Purbawinata, M.A., Ratdomopurbo, A., Sinulingga, I.K., Sumarti, S. & Suharno, eds, 1996. *Merapi Volcano—a Guide Book,* Direktorat Vulkanologi, Bandung, Indonesia.

Ratdomopurbo, A., 1995. Etude sismologique du volcan Merapi et formation du dôme de 1994, *PhD thesis,* L'université Joseph Fourier, Grenoble (in French).

Sato, H., 1977. Energy propagation including scattering effect; single isotropic scattering approximation, *J. Phys. Earth,* **25,** 27–41.

Sato, H., 1993. Energy transportation in one- and two-dimensional scattering media: analytic solutions of the multiple isotropic scattering model, *Geophys. J. Int.,* **112,** 141–146.

Sato, H. & Fehler, M.C., 1998. *Seismic Wave Propagation and Scattering in the Heterogeneous Earth,* Springer-Verlag, New York.

Schwarzkopf, L., Schmincke, H.-U. & Freundt, A., 1998. Eruptive mechanisms of Merapi volcano during the 20th century with emphasis on structure and transport of the block-and-ash flow of 1994, in *Decade-Volcanoes under Investigation,* Vol. Sonderband III/1998 of DGG-Mitteilungen, pp. 21–24, eds Zschau, J. & Westerhaus, M., Deutsche Geophysikalische Gesellschaft.

Simkin, T., Siebert, L., McClellard, L., Bridge, D., Newhall, C. & Latter, J., 1981. *Volcanoes of the World,* Geoscience Press, Tucson, AZ.

Van Tiggelen, B.A., 1999. Localization of waves, in *Diffuse Waves in Complex Media*, pp. 1–60, ed. Fouque, J.-P., Kluwer Academic, Dortrecht.

Wassermann, J., Budi, E., Ohrnberger, M. & Gossler, J., 1999. Long term seismicity and source changes during different activity stages of Mt. Merapi (Indonesia) using a two scale seismic array, in *IUGG Abstracts,* vol. B, p. 156, Birmingham, UK.

Weaver, R.L., 1990. Anderson localization of ultrasound, *Wave Motion,* **12,** 129–142.

Wegler, U., 1999. Deterministische und statistische Untergrundmodelle des Vulkans Merapi (Java, Indonesien)—eine Analyse künstlich erzeugter seismischer Signale, *PhD thesis,* Mathematisch-Naturwissenschaftliche Fakultät der Universität Potsdam (in German).

Wegler, U. & Seidl, D., 1997. Kinematic parameters of the tremor wave field at Mt. Etna (Sicily), *Geophys. Res. Lett.,* **24,** 759–762.

Wegler, U., Lühr, B.-G. & Ratdomopurbo, A., 1999. A repeatable seismic source for tomography at volcanoes, *Ann. Geofis.,* **42,** 565–571.

Wesley, J.P., 1965. Diffusion of seismic energy in the near range, *J. geophys. Res.,* **70,** 5099–5106.

Wilson, M., 1989. *Igneous Petrogenesis: a Global Tectonic Approach,* Unwin Hyman, London.

Wu, R., 1985. Multiple scattering and energy transfer of seismic waves; separation of scattering effect from intrinsic attenuation; i. theoretical modelling, *Geophys. J. R. astr. Soc.,* **82,** 57–80.

Wu, R. & Aki, K., 1985. Elastic wave scattering by a random medium and the small-scale inhomogeneities in the lithosphere, *J. geophys. Res.,* **90,** 10 261–10 273.

Yamamoto, K. & Ida, Y., 1997. Significant P wave attenuation for a specific frequency range beneath Kirishima volcano, Japan, *Geophys. Res. Lett.,* **24,** 1275–1278.

Zeng, Y., 1993. Theory of scattered P - and S-wave energy in a random isotropic scattering medium, *Bull. seism. Soc. Am.,* **83,** 1264–1976.

Zeng, Y., Su, F. & Aki, K., 1991. Scattering wave energy propagation in a random isotropic scattering medium: 1. Theory, *J. geophys. Res.,* **96,** 607–619.

Zschau, J. & Westerhaus, M., 1998. *Decade-Volcanoes under Investigation,* Vol. Sonderband III/1998 of DGG-Mitteilungen, Deutsche Geophysikalische Gesellschaft.

Zschau, J., Sukhyar, R., Purbawinata, M.A., Lühr, B. & Westerhaus, M., 1998. Project MERAPI—interdisciplinary research at a high-risk volcano, in *Decade-Volcanoes under Investigation,* Vol. Sonderband III/1998 of DGG-Mitteilungen, pp. 3–8, eds Zschau, J. & Westerhaus, M., Deutsche Geophysikalische Gesellschaft.